ACE2 nanoparticles prevent cell entry of SARS-CoV-2

Cécile Sauvanet[1,2], Moara Lemos[1,2], Armel Bezault[1,2], Borja Rodríguez de Francisco[1,2], Michael CW Chan[3,4], Kenrie PY Hui[3,4], Ka-chun Ng[3], John M Nicholls[5], Niels Volkmann[2*] and Dorit Hanein[6]

[1]Structural Studies of Macromolecular Machines in Cellulo Unit, Department of Structural Biology and Chemistry, Institut Pasteur, Université Paris Cité, CNRS UMR3528, Paris, France.

[2]Structural Image Analysis Unit, Department of Structural Biology and Chemistry, Institut Pasteur, Université Paris Cité, CNRS UMR3528, Paris, France.

[3]School of Public Health, Li Ka Shing Faculty of Medicine, The University of Hong Kong, Pokfulam, Hong Kong SAR, China.

[4]Centre for Immunology and Infection (C2i), Hong Kong Science Park, Hong Kong SAR, China.

[5]Department of Pathology, School of Clinical Medicine, Li Ka Shing Faculty of Medicine, The University of Hong Kong, Pokfulam, Hong Kong SAR, China

[6]Scintillon Institute, San Diego, CA, USA

*Corresponding author: Niels Volkmann (niels.volkmann@pasteur.fr)

We have now been in the grip of the COVID-19 pandemic for over two years with devastating consequences. The continual evolution of the virus has challenged the efficacy of many vaccines and treatment options based on immunotherapies are compromised by this viral escape. One treatment strategy that averts viral escape is the use of constructs based on its entry receptor Angiotensin-Converting Enzyme 2 (ACE2) acting as decoys. Here, we combined full-length human ACE2 with viral vectors commonly used for gene therapy to form nanoparticles that present ACE2 on their surface analogous to human cells. Using cell-based assays and direct, multiscale imaging including cryogenic cellular tomography, we show that these ACE2 nanoparticles are highly efficient in preventing entry of SARS-CoV-2, the virus causing COVID-19, in model cell systems as well as human respiratory tract *ex-vivo* cultures. Thus, ACE2 nanoparticles have high potential as the next generation therapeutics for addressing the immediate needs of the current pandemic and possible future outbreaks.

The COVID-19 pandemic is wreaking havoc on health and economy on a global scale. The disease is caused by infections with sudden emergence of severe acute respiratory syndrome coronavirus 2 (SARS-CoV-2)[1]. The virus enters human cells via interactions between its spike protein and the human angiotensin-converting enzyme 2 (hACE2)[2]. The virus can enter through membrane fusion, which also requires the presence of Transmembrane Serine Protease 2

(TMPRSS2)[3], or through the clathrin-mediated endocytic pathway[4]. In either case, the presence of hACE2 on the cell surface is obligatory for viral entry.

Several vaccines and treatment approaches have been developed against SARS-CoV-2. Most of these options rely on the actions of antibodies that bind to exposed viral proteins and prevent cell entry. A major concern with this strategy has been the development of different naturally evolving variants of SARS-CoV-2 that diminish the interactions between its proteins and antibodies, thus compromising the efficiency of vaccines and treatments. This viral escape mechanism is currently in action with the Omicron variant, which carries 15 mutations in the ACE2 receptor binding domain alone[5], and significantly weakens the efficiency of vaccines[6] and antibody treatments[7].

Other treatment options target the viral replication process where the drug interferes by binding to the viral protease or to the viral polymerase[8]. Because these inhibition mechanisms also involve binding to viral proteins, which can be subject to mutations, this strategy is also prone to be affected by viral escape. In addition, drugs that are targeting the replication process are potentially more likely to cause side effects because they act inside the cell rather than preventing viral entry all together. For example, the protease inhibitor Molnupiravir has raised concerns about potential long-term side effects including cancer and birth defects[9].

One viable strategy to combat viral escape is to make use of the obligatory entry receptor, in this case hACE2, as a decoy to prevent viral entry. Even heavily mutated viruses must preserve their ability to bind to this receptor in order to enter their target cells. Presenting hACE2 outside the cell engages the virus, diminishing its cell entry capacity[10].

Here, we targeted SARS-CoV-2 cell entry by constructing an efficient decoy that involves a carrier system based on murine leukaemia virus (MLV), which has been extensively used as a viral vector in gene therapy studies[11], pseudotyped with full-length hACE2 on its surface (hACE2 nanoparticles). To monitor the effect of hACE2 nanoparticles on SARS-CoV-2 entry using luciferase activity assays[12], we also generated MLVs carrying luciferase mRNA (control MLVs) and pseudoviruses[13] composed of control MLVs pseudotyped, with wild-type SARS-CoV-2 spike protein, delta-variant spike, or omicron-variant spike.

Following pseudovirus infection, we used cellular cryogenic electron tomography (cryo-ET) to verify the morphology of pseudoviruses and their presence inside Vero-E6 African green monkey kidney cells. Vero-E6 cells are known to support SARS-CoV-2 replication and were shown to report accurately on SARS-CoV-2 pseudovirus infection rates[14]. They endogenously express African green monkey ACE2, which shares 100% sequence identity with hACE2. The presence of SARS-CoV-2 spikes in both the pre- and post-fusion configurations protruding from the pseudovirus surface are clearly visible (Figure 1a-d and 1b inset). The structural signature of the pseudovirus capsid is highly distinct (Figure 1a insets), facilitating identification of the pseudovirus not only outside but also within cells. Our analysis of pseudoviruses inside Vero-E6 cells revealed that pseudovirus cell entry is accomplished via the clathrin-mediated endocytic pathway (Figure 1 c-e). This mechanism is consistent with entry of SARS-CoV-2 in the absence of TMPRSS2[3] and is the preferred pathway of entry for the omicron variant [6].

Next, we verified that hACE2 is required for entry of these pseudoviruses using luciferase activity assays with the Baby Hamster Kidney fibroblasts 21 (BHK-21) cell system[14] (schematic depiction Figure 1f). We used parental BHK-21 cells, which lack hACE2, or BHK-21 cells transiently expressing hACE2 to show that pseudoviruses only enter cells that carry hACE2 (Figure 2a). To quantify the effect of hACE2 nanoparticles on pseudovirus cell entry we conducted luciferase activity assays with the Vero-E6 system. We found that the presence of hACE2 nanoparticles reduces the amount of pseudovirus cell entry by 97.6% for wild-type SARS-CoV-2 pseudoviruses, 97.4% for delta-variant pseudoviruses, and 99.3% for omicron-variant pseudoviruses (Figure 2b and c). Quantification of the hACE2 concentration on the nanoparticles (Figure 2d and e) showed that the entry suppression of hACE2 in the context of nanoparticles is between one and two orders of magnitude more efficient than soluble hACE2 to achieve similar viral entry neutralization.

Next, we tested the effect of hACE2 nanoparticles on the viral replication kinetics of SARS-CoV-2 delta variant in *ex vivo* cultures of human bronchus tissues[15]. This presents a near real-life scenario of human SARS-CoV-2 delta variant infection, the most clinically significant variant so far[16]. We found that the presence of hACE2 nanoparticles abolishes viral replication down to the level of detectability (Figure 3).

To elucidate the mechanism of hACE2 nanoparticles entry inhibition, we employed cryo-ET to characterize the hACE2 nanoparticles and their interactions with SARS-CoV-2 pseudoviruses. Structural analysis of the hACE2 nanoparticles revealed a high density of particles protruding from the MLV membrane that are fully consistent with the structure of membrane-embedded ACE2 dimers[17] (Figure 4 a and b). Interactions between pseudoviruses and hACE2 nanoparticles are clearly facilitated by interactions between pre-fusion spikes and hACE2 dimers, leading to engagement of pseudoviruses with the hACE2 nanoparticles and aggregates crosslinked by hACE2-spike interactions (Figure 4c and insets).

hACE2 nanoparticles are highly efficient in preventing infection of Vero-E6 cells by SARS-CoV-2 pseudoviruses as well as infection by live SARS-CoV-2 virus of *ex vivo* human bronchus tissue via competition of membrane-embedded receptors in the nanoparticles with cell receptors as well as crosslinking through the engagement of receptors on the same nanoparticle with multiple viruses. Our studies suggest that hACE2 nanoparticles provide a potent and effective decoy with strong viral entry neutralization effect and thus present a promising opportunity to develop a new generation of COVID19 treatment options that are much less prone to viral escape than current strategies. The *ex-vivo* results show that the efficiency of inhibition by hACE2 nanoparticles remains high even if the concentration is reduced by two orders of magnitude. Soluble hACE2 constructs have been shown to be well tolerated in clinical trials[18] and MLV-based particles have a long history of clinical applications in the context of viral gene therapy[19]. The hope is that our studies, combined with these practical facts will trigger and accelerate the development of preventative as well as early stage COVID19 therapeutics based on hACE2 nanoparticles.

REFERENCES

1. Zhou, P. et al. A pneumonia outbreak associated with a new coronavirus of probable bat origin. *Nature* **579**, 270-273 (2020).
2. Shang, J. et al. Structural basis of receptor recognition by SARS-CoV-2. *Nature* **581**, 221-224 (2020).
3. Koch, J. et al. TMPRSS2 expression dictates the entry route used by SARS-CoV-2 to infect host cells. *EMBO J* **40**, e107821 (2021).
4. Bayati, A., Kumar, R., Francis, V. & McPherson, P. S. SARS-CoV-2 infects cells after viral entry via clathrin-mediated endocytosis. *J Biol Chem* **296**, 100306 (2021).
5. Mannar, D. et al. SARS-CoV-2 Omicron variant: Antibody evasion and cryo-EM structure of spike protein-ACE2 complex. *Science* **375**, 760-764 (2022).
6. Meng, B. et al. Altered TMPRSS2 usage by SARS-CoV-2 Omicron impacts infectivity and fusogenicity. *Nature* **603**, 706-714 (2022).
7. Cao, Y. et al. Omicron escapes the majority of existing SARS-CoV-2 neutralizing antibodies. *Nature* **602**, 657-663 (2022).
8. Vangeel, L. et al. Remdesivir, Molnupiravir and Nirmatrelvir remain active against SARS-CoV-2 Omicron and other variants of concern. *Antiviral Res* **198**, 105252 (2022).
9. Zhou, S. et al. β-d-N4-hydroxycytidine Inhibits SARS-CoV-2 Through Lethal Mutagenesis But Is Also Mutagenic To Mammalian Cells. *J Infect Dis* **224**, 415-419 (2021).
10. Jing, W. & Procko, E. ACE2-based decoy receptors for SARS coronavirus 2. *Proteins* **89**, 1065-1078 (2021).
11. Yoder, K. E., Rabe, A. J., Fishel, R. & Larue, R. C. Strategies for Targeting Retroviral Integration for Safer Gene Therapy: Advances and Challenges. *Front Mol Biosci* **8**, 662331 (2021).
12. Brasier, A. R. & Ron, D. Luciferase reporter gene assay in mammalian cells. *Methods Enzymol* **216**, 386-397 (1992).
13. Millet, J. K. & Whittaker, G. R. Murine Leukemia Virus (MLV)-based Coronavirus Spike-pseudotyped Particle Production and Infection. *Bio Protoc* **6**, (2016).
14. Walls, A. C. et al. Structure, Function, and Antigenicity of the SARS-CoV-2 Spike Glycoprotein. *Cell* (2020).
15. Chan, M. C. et al. Tropism and innate host responses of a novel avian influenza A H7N9 virus: an analysis of ex-vivo and in-vitro cultures of the human respiratory tract. *Lancet Respir Med* **1**, 534-542 (2013).
16. Bast, E., Tang, F., Dahn, J. & Palacio, A. Increased risk of hospitalisation and death with the delta variant in the USA. *Lancet Infect Dis* **21**, 1629-1630 (2021).
17. Yan, R. et al. Structural basis for the recognition of SARS-CoV-2 by full-length human ACE2. *Science* **367**, 1444-1448 (2020).
18. Khan, A. et al. A pilot clinical trial of recombinant human angiotensin-converting enzyme 2 in acute respiratory distress syndrome. *Crit Care* **21**, 234 (2017).
19. Rodrigues, A. F., Alves, P. M. & Coroadinha, A. S. in *Viral gene therapy* (ed Xu, K.) 15-40 (IntechOpen, London, UK, 2011).

FIGURES

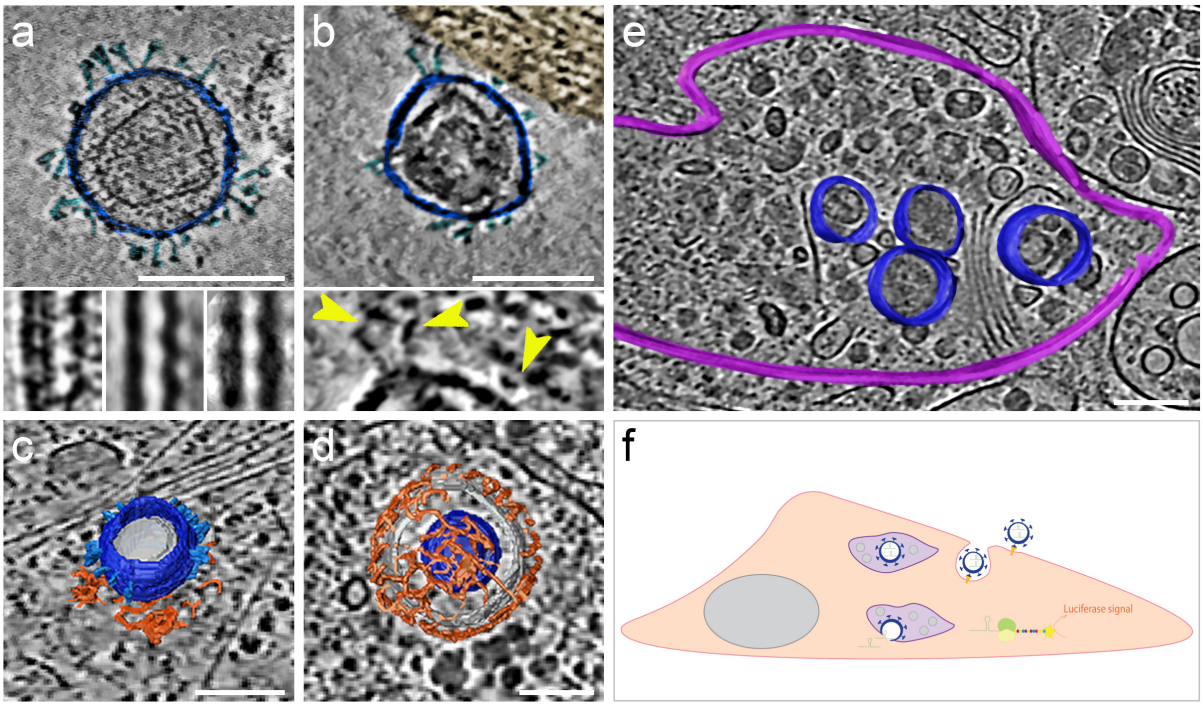

Figure 1: **SARS-CoV-2 pseudoviruses enter cells via the clathrin-mediated endocytotic pathway.** Cryo-ET reveals pseudovirus morphology and entry mechanism into Vero-E6 cells. Pseudovirus membranes and their segmentation are coloured dark blue. Spikes are coloured light blue. Clathrin triskeletons are coloured in orange, endolysosomal membrane in purple. All virtual slices are 12 nm thick. All scale bars = 100 nm. (a) Slice through a tomogram showing a pseudovirus. SARS-CoV-2 spikes are clearly identifiable. The pseudoviruses carry a distinct structural signature imposed by the MLV capsid lattice. The insets show the ridge like structure in a raw slice (left) and after averaging outside (centre) and inside (right) the cell. (b) Slice through a region of interaction between cell plasma membrane and a pseudovirus. The cell region, tinted gold, shows actin filaments running parallel to the plasma membrane. The inset shows a close-up view with yellow arrowheads pointing at connections between the membrane and the SARS-CoV-2 spikes of the pseudovirus. (c) Surface representation of a pseudovirus in the process of entering, attached to a clathrin-coated pit. A slice of the underlying tomogram is superimposed in the background for reference SARS-CoV-2. (d) Surface representation of a SARS-CoV-2 pseudovirus inside a clathrin-coated vesicle. A slice of the underlying tomogram is superimposed in the background for reference. (e) Surface representation of an endolysosomal compartment containing several pseudoviruses. A slice of the underlying tomogram is shown for reference and represents several loaded vesicles and convoluted membrane structures. (f) Schematic representation of SARS-CoV-2-pseudovirus entry and the subsequent steps leading to luciferase signals. Pseudoviruses bind hACE2 receptors via their SARS-CoV-2 spikes on the cell surface (b), which triggers endocytosis (c, d). Once inside, these pseudoviruses are targeted to the endolysosomal system (purple, e) allowing the release of luciferase mRNA. The resulting bioluminescent (yellow star) is proportional to the amount of pseudoviruses that entered the cell (Figure 2).

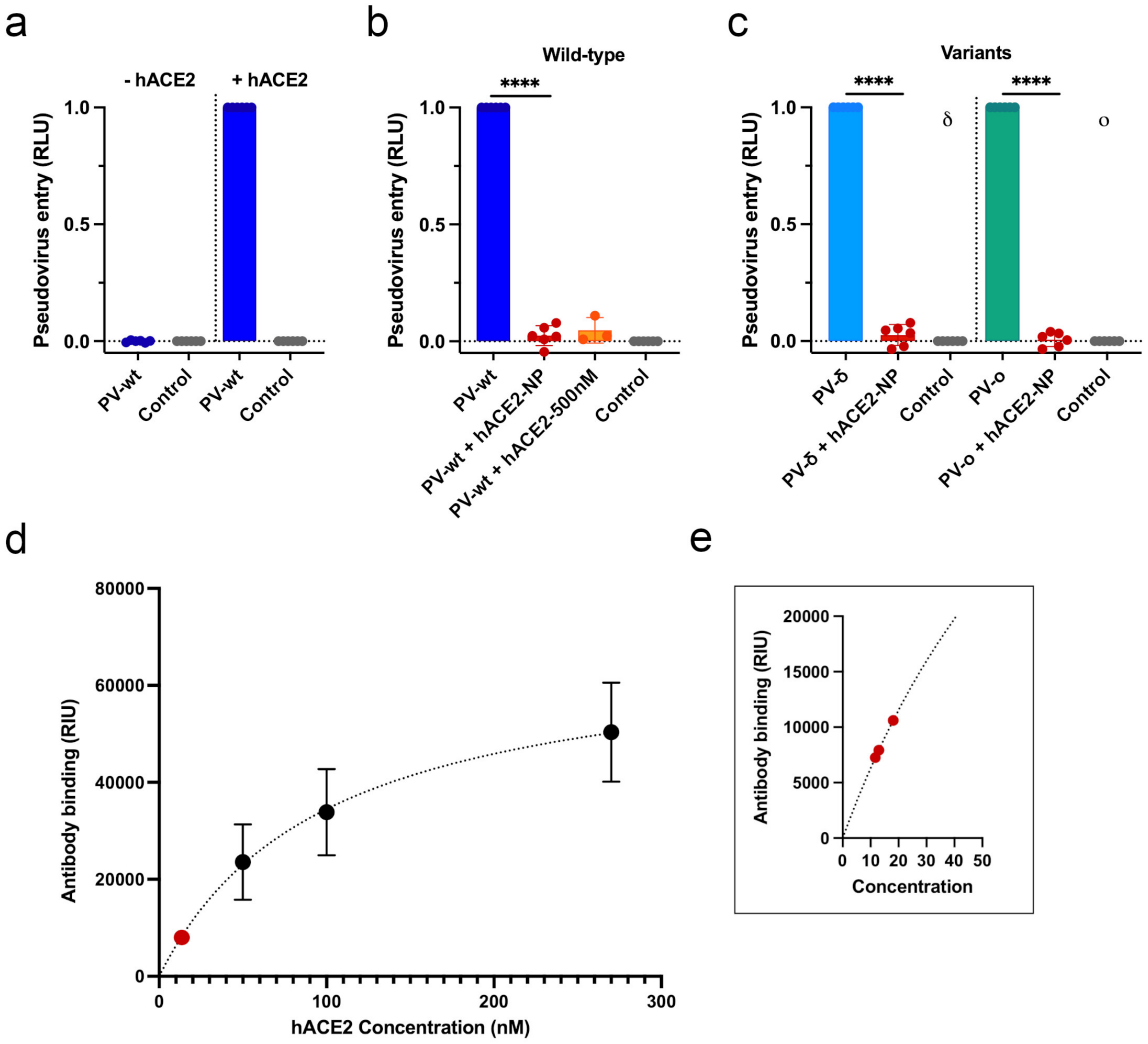

Figure 2: **hACE2 nanoparticles block SARS-CoV-2 pseudovirus entry**. (a) Luciferase activity assays were performed after overnight incubation of parental BHK-21 cells (-hACE2) or hACE2-expressing BHK-21 cells (+hACE2) with wild-type pseudoviruses (PV-wt). SARS-CoV-2 pseudoviruses enter cells and generate a luciferase signal only for cells expressing hACE2. All luciferase data were normalized to correspond to zero for the signal from control MLVs only carrying luciferase mRNA (Control) and set to one for the signal from pseudovirus only. The bars represent the mean ± standard deviation of experimental replicates. (b) Luciferase activity assays of Vero-E6 cells with wild-type pseudovirus (PV-wt) in the absence and presence of hACE2 nanoparticles (hACE2-NP) or 500nM soluble hACE2 (hACE2-500nM). (c) Luciferase activity assays of Vero-E6 cells with delta-variant (PV-*δ*) or omicron-variant (PV-o) pseudovirus in the absence and presence of hACE2 nanoparticles (hACE2-NP). Entry of pseudoviruses into Vero-E6 cells is blocked by hACE2 nanoparticles for all variants including wild type. (d) Quantification of hACE2 level in hACE2 nanoparticles by western blot (Extended Data Figure 1). The curve plots the intensity of the signal from hACE2 antibodies versus the corresponding concentration of soluble hACE2. The red dot marks the average location of the hACE2 nanoparticle intensities. (e) Intensities from three independent samples of hACE2 nanoparticles overlaid on the calibration curve used to extrapolate hACE2 concentration.

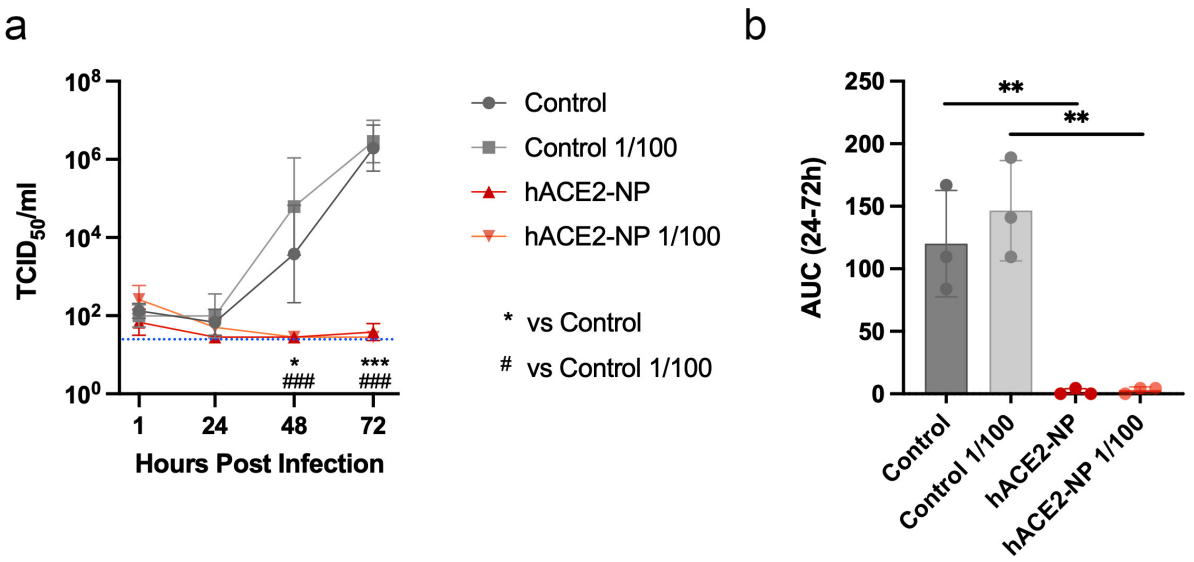

Figure 3: hACE2 nanoparticles block SARS-CoV-2 virus entry in *ex vivo* human bronchus explants. Effect of hACE2 nanoparticles on the viral replication kinetics of SARS-CoV-2 delta variant in *ex-vivo* cultures of human bronchus . Human *ex-vivo* explant cultures of bronchus were pre-treated with control MLVs (Control) or hACE2 nanoparticles (hACE2-NP; neat or 1/100 diluted) and then infected with delta-variant SARS-CoV-2 viruses at 37°C. Virus released in the culture supernatants were measured over time by $TCID_{50}$ assays. (a) Viral replication kinetics of Delta in human *ex vivo* cultures of bronchus. The horizontal blue dotted line denotes the limit of detection in the $TCID_{50}$ assay. Data are presented as geometric mean values (n=3) (±SD). Statistics were performed using Two-way ANOVA followed by Tukey's test. *$p<0.05$, ***$p<0.001$ vs control MLVs; ###$p<0.001$ vs control MLVs 1/100. (b) Viral titers are depicted as area under the curve (AUC). Bar-charts show the mean (n=3) (±SD). Statistics were performed using One-way ANOVA followed by a Tukey's multiple-comparison test. **$p<0.01$.

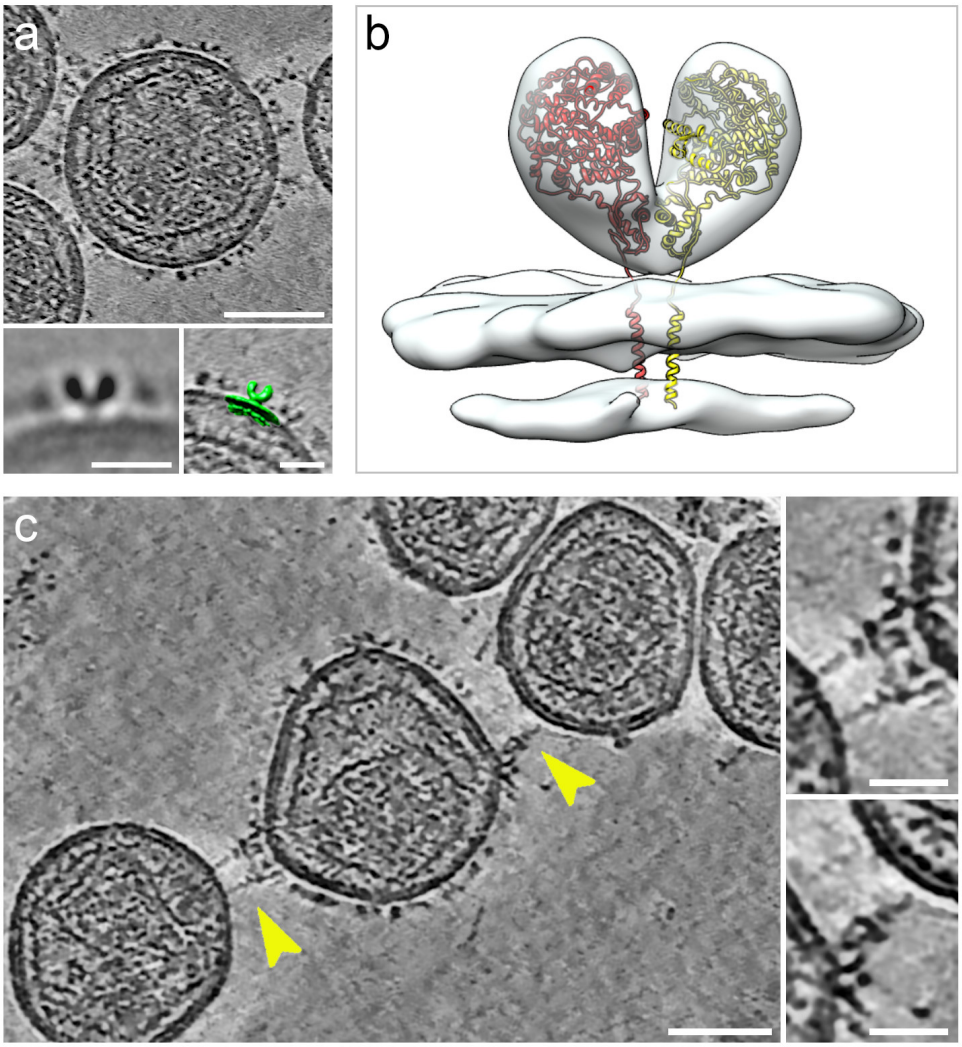

Figure 4: **Cryogenic electron tomography of hACE2 nanoparticles reveals their interaction with SARS-CoV-2 pseudoviruses.** All virtual slices in this figure are 12-nm thick. Bars in main panels = 50 nm; bars in insets = 20 nm. (a) Slice through a tomogram of an hACE2 nanoparticle showing dense decoration with hACE2 dimers. Insets show two-dimensional average of the protein density protruding from the nanoparticles (left) and overlay with surface representation (green) of three-dimensional (3D) reconstruction of membrane-bound particles (right). (b) Surface representation of 3D reconstruction obtained by sub-tomogram averaging of membrane-bound particles (Extended Data Figure 2). The atomic structure of the ACE2 dimer (monomers in yellow and red), extracted from the open conformation of the hACE2-B0AT1 complex (PDB: 6MD1), was fitted into the density showing a good match. (c) Virtual slice through a tomogram of hACE2 nanoparticles interacting with SARS-CoV-2 pseudoviruses. Interactions between hACE2 and spikes are marked with yellow arrowheads. Insets show close-up views of interactions between hACE2 nanoparticles and spike marked by the yellow arrowheads.

METHODS

Cell lines

Human primary embryonic kidney 293T/17 (HEK293T/17) cells, monkey kidney Vero E6 cells (Vero-E6), and Baby hamster kidney fibroblast 21 (BHK-21) cells were obtained from the American Type Culture Collection (ATCC® CRL-11268, ATCC® CRL-1586™, ATCC® CCL-10™). HEK293T/17 cells were maintained in a humidified 5% CO_2 incubator in complete Dulbecco's Modified Eagle Medium (DMEM) supplemented with 100 U/ml penicillin, 100 µg/ml streptomycin, 10 mM 4-(2-hydroxyethyl)-1-piperazineethanesulfonic acid (HEPES), and 10% fetal bovine serum (FBS) (Sigma-Aldrich). HEK293T/17 cells were used to produce pseudoviruses with spike protein from wild-type SARS-CoV-2, delta variant, and omicron variant. HEK293T/17 cells were also used to produce MLV control and hACE2 nanoparticles. Vero E6 and BHK-21 were maintained at 37°C with 5% CO_2 incubator in Modified Eagle Medium (MEM) supplemented with 1X non-essential amino acid, 2mM L-glutamine, 100 U/ml penicillin, 100 µg/ml streptomycin, and 10% FBS (all from Sigma-Aldrich). All cell lines were tested for mycoplasma every three months using the Lookout Mycoplasma PCR detection kit (Sigma-Aldrich) and were authenticated by ATCC®.

Plasmids

The plasmids for MLV production, pCMV-MLV-gag-pol and pTG-Luc, were kindly provided by Jean Dubuisson (Institut Pasteur de Lille). pcDNA3.1-SARS2-Spike[1] and pcDNA3.1-hACE2[1] were obtained from Addgene (Addgene plasmids #145032; #145033); pCI-SARS2-Spike expressing a codon optimized version of the gene coding for S protein of SARS-CoV-2 was provided by Nicolas Escriou (Institut Pasteur). pUNO1-SpikeV8 carrying delta variant spike and pUNO1-SpikeV11 carrying omicron (B.1.1.529/BA.1 lineage) spike were purchased from InvivoGen (catalogue numbers p1-spike-v8 and p1-spike-v11 respectively).

Pseudovirus and hACE2 nanoparticles production

Control MLVs, MLV-based pseudoviruses carrying SARS-CoV-2 wild-type, delta, or omicron spike protein, and MLV-based hACE2 nanoparticles were prepared as previously described[2]. In brief, HEK-293T/17 cells were co-transfected using Lipofectamine 2000 (Life Technologies) with MLV Gag-Pol packaging construct and the MLV transfer vector encoding a luciferase gene reporter either by itself (MLV-control) or with one of the Spike protein or hACE2 protein expression vectors for 48h at 37°C or 72h at 33°C. The resulting particles were released in the supernatant, which was then harvested and filtered through 0.45µm membranes, aliquoted and stored at -80 °C.

Pseudovirus cell entry assays

Vero-E6 and BHK-21 cells were plated into 24 wells at a dilution of 5 x 10^5 cell/ml. One day prior, 60mm dish of BHK-21 cells were transiently transfected with 2.5 µg human ACE2 or no DNA for control using standard lipofectamine 2000 (Life Technologies) protocols. After 24hrs, 200 µl of pseudovirus were added to the wells, after washing 3X in DPBS, incubated for 1h at 37°C in 5% CO_2 incubator before adding 300µl of complete MEM over a day (7hrs) or for overnight incubation. Cells were washed in MEM without serum, and 100 µl One-Glo-EX (Promega) was added to the cells in equivalent MEM no serum volume and incubated in the dark for 5 min. 180µl of the mixture was moved to 96 well plates prior to reading. For the competition

assays, experiments were performed in 96 wells plates. Prior to cell infection, 40 µL of hACE2 nanoparticles or the desired concentration of soluble hACE2 (provided by Ignacio Fernández and Félix Rey, Institut Pasteur) were added to the cell culture, incubated for 30min before addition of pseudoviruses (40 µl). After an additional 30 min of incubation, full media was added to pursue overnight incubation. The luciferase signal was determined in a Varioskan LUX microplate reader (Thermo Fisher Scientific) at 10 readings for each well at intervals of 30 s. Measurements were done in triplicate. A slight increase of luciferase activity was observed after 7hrs of interaction but to observe the potent effect of hACE2 nanoparticles overnight incubation was chosen as reference point. Relative luciferase units (RLU) data were normalized to pseudovirus signal set to one and the signal from controls without pseudovirus set to zero. All normalized data were then statistically analysed and represented using GraphPad Prism, version 9.3.1 (GraphPad Software).

Western Blotting

hACE2 nanoparticles and soluble hACE2 were thawed and 4X SDS loading buffer was added prior to boiling for 5 min at 95°C. The same quantity of samples used for the competition assay were run on a 4%–20% gradient Tris-Glycine Gel (BioRad) and transferred to nitrocellulose membrane. A Goat anti-hACE2 polyclonal primary antibody (at 1:100 dilution corresponding to a concentration of 2 µg/ml; Bio-techne, catalogue number #AF933) and an Alexa Fluor 488-conjugated donkey anti-goat secondary antibody (1:10,000 dilution, Jackson Laboratory, Catalog number # 305-547-003) were used for Western-blotting. Western blots were imaged using a BioRad ChemiDoc MP Imaging System.

SARS-CoV-2 delta variant isolation

Delta (B.1.617.2, hCoV-19/Hong Kong/CM21000383_WHP4738/2021) variant was isolated and propagated in Vero-E6-TMPRSS2 overexpressing cells[3]. The cell-line was cultured in DMEM with 10% FBS. The original clinical specimen was collected from SARS-CoV-2 confirmed patients in Hong Kong in 2021 and isolated as previously described[4]. The virus stock was aliquoted and stored frozen at -80°C. Aliquots were titrated to determine plaque forming units. The experiments were carried out in a Bio-safety level 3 (BSL-3) facility at the School of Public Health, LKS Faculty of Medicine, The University of Hong Kong.

Ex-vivo cultures and infection of human bronchus tissues

Fresh non-tumour bronchus tissues were obtained from patients undergoing elective surgery in Department of Surgery at Queen Mary Hospital (Pok Fu Lam, Hong Kong, China) and were removed as part of routine clinical care but surplus for routine diagnostic requirements as detailed previously[5,6]. The virus infection procedures were performed as previously described[5]. Briefly, similar sized pieces of human bronchus tissues were treated with MLV-control or hACE2 nanoparticles for 30 min at 37°C and then infected with SARS-CoV-2 at $4x10^4$ plaque forming units for 1 h at 37°C. Each tissue fragment was washed three times to remove residual virus inoculum and incubated at 37°C with fresh medium. Aliquots of culture medium were removed at times indicated and stored at -80°C until titration. Infectious viral titers in culture supernatants were assayed by $TCID_{50}$ in Vero-E6-TMPRSS2 cells. Informed consent for the use of human tissues was obtained from all subjects and approval was granted by the Institutional Review Board (IRB) of the University of Hong Kong and the Hospital Authority (Hong Kong West) (IRB approval no: UW 20-862).

Viral titration by $TCID_{50}$ assay

Vero-E6-TMPRSS2 cells were seeded in 96-well tissue culture plates one day before the virus titration ($TCID_{50}$) assay. Cells were washed once with PBS and DMEM (Gibco) with 2% foetal bovine serum (Gibco) supplemented with 100 units/ml penicillin and 100 µg/ml streptomycin (Gibco) was added. Serial dilutions of virus supernatant, from 0.5 log to 7 log, were performed and each virus dilution added to the plates in quadruplicate. The plates were observed for cytopathic effect daily. The end point of viral dilution leading to CPE in 50% of inoculated wells was estimated using the Karber method[7]. Area under the curve (AUC) was calculated from the viral titers from different time points indicated on the Y-axis.

Quantification and Statistical Analysis

For western blots and luciferase activity assays, experiments were performed multiple times with at least two independent preparations of each sample. Quantification of the intensity of western blot bands was realized by densitometric analysis using Fiji[8], version 2.1.0. Soluble hACE2 samples of different concentrations were used to establish a standard curve, which was used to determine hACE2 level on the nanoparticles. Luciferase data from individual experiments were background corrected by subtracting the signal from control MLVs and then normalized by setting the background corrected signal from unperturbed pseudovirus to one. One-sided, one-tailed t-tests were performed against 1 and 0 for all other normalized, background-corrected conditions; two-tailed t-tests were used to compare the normalized, background corrected signals from pseudovirus in the presence of hACE2 nanoparticles (hACE2-NP) or soluble hACE2. Significance of differences was determined after Bonferroni correction. The difference between pseudovirus alone and pseudovirus in the presence of hACE2-NP was statistically highly significant (wild-type p-value: $1.73\ e^{-8}$; delta p-value: $2.18\ e^{-8}$; omega p-value: $2.66\ e^{-9}$) and there was no statistically significant difference with Control (wild-type p-value: 0.11; delta p-value: 0.10; omega p-value: 0.30). There was no statistically significant difference between wild-type pseudovirus in the presence of hACE2-NP and 500nM soluble hACE2 (p-value: 0.50). The difference between parental BHK-21 cells in the presence and absence of wild-type pseudovirus was not significant (p-value: 0.37) and the difference between parental and hACE2-expresing BHK-21 cells in the presence of wild-type pseudovirus was highly significant (p-value: $1.57\ e^{-13}$). Statistics for the $TCID_{50}$ assays were performed using two-way ANOVA followed by Tukey's test. Statistics for the AUC analysis was performed using One-way ANOVA followed by a Tukey's multiple-comparison test.

Cryo-ET sample preparation of MLV-based samples

Pseudovirus samples were concentrated 10 to 20 times by ultracentrifugation (Optima MAX-XP Ultracentrifuge; Beckman Coulter) for 30 min, at 4°C in a TLA-55 rotor (Beckman Coulter) at maximum speed (186000g) then resuspended in similar media overnight at 4°C. Samples were fixed in 4% formaldehyde (Tousimis Research Corporation; catalogue number #1008A) diluted in full media for 30 min at 37°C then stored at 4°C. For vitrification, samples were loaded onto plasma cleaned (Solarus II Plasma Cleaner; Gatan, Inc.) Holey Carbon Film R 1.2/1.3 Copper 400 mesh EM grids (Quantifoil Micro Tools GmbH; catalogue number #N1-C14nCu40-01;), incubated for 30 secs prior to plunge freezing in liquid ethane either using a manual plunger or a Vitrobot Mark IV system (Thermo Fisher Scientific). For mixtures between pseudoviruses and hACE2 nanoparticles, the samples were resuspended in similar media for 2-3hrs. Mixtures of

pseudovirus and hACE2 nanoparticles (1:1 volume) were incubated for 30 min at 37°C prior to vitrification. Samples without fixation were loaded on freshly glow discharged (Leica EM ACE600) EM grids both vitrified with a Vitrobot Mark IV system and imaged at the IRBA facility. For all samples ~1 µl of 5-nm protein A Gold (UMC Utrecht) were added as fiducial markers to assist with tilt series alignment.

Cryo-ET data collection of MLV-based samples

Data were acquired on a Titan Krios G3i (Thermo Fisher Scientific) operated at 300kV in parallel beam condition, a K3 Summit direct electron detection device and a BioQuantum energy filter (Gatan Inc.) operated in zero-loss mode with a slit width of 20 eV. Automated data collection was carried out using SerialEM[9], version 3.8, at a nominal magnification of 42K x with a calibrated pixel size of 2.1 Å. Tilt series were acquired following the dose symmetric scheme[10] between +60° and -60° with a step size of 3°. The dose rate was adjusted to 23 counts/pixel/s resulting in a total dose of $100e^-/Å^2$ per tilt series, and each tilt image was acquired in electron counting mode and fractionated in 13 to 14 frames. The defocus range was -5 to -8 µm. Data was also acquired on a Titan Krios G3i operated at 300 kV in parallel beam condition, and a Falcon 3EC direct electron detection device, at a nominal magnification of 37K with a calibrated pixel size of 2.3 Å using Tomography software (Thermo Fisher Scientific) and the same set of parameters as above.

Cryo-ET sample preparation of pseudovirus-infected cells

Vero-E6 were seeded on holey carbon film R 5/20 gold 200 mesh EM grids (Quantifoil Micro Tools GmbH; catalogue number # N1-C43cAuE1-01) at a cell density of 5000 cells per grid, incubated in complete media up to 24 hrs at 37˚C in 5% CO_2 incubator. Pseudoviruses were then incubated with the cells from 30 min to overnight. Cells were washed in MEM without serum and then fixed in a structure-preserving buffer[11] (0.1 M Pipes, 1 mM EGTA, and 1 mM $MgSO_4$) containing formaldehyde 4% for 30 min at 37˚C. Plasma membranes of cells were stained for light microscopy using WGA 647 according to supplier protocol (Invitrogen, Thermo Fisher Scientific). Grids were then stored at 4°C in PHEM buffer and 1% formaldehyde. Next, the grids were screened for cell-density and integrity on a DMi8 light microscope (Leica Microsystems). Samples that passed the screening were vitrified in liquid-nitrogen cooled liquefied ethane using either a manual plunger, Vitrobot Mark IV system (Thermo Fisher Scientific) or EM GP Model 1 plunge freezer (Leica Microsystems). For all samples, 1µl of 10 nm protein A Gold (UMC Utrecht) were added as fiducial markers to assist with tilt series alignment. The vitrified grids were then mounted into grid support rings (Auto-gridTEM sample holder, Thermo Fisher Scientific), and transferred to a cryogenic light microscopy (cryo-LM) shuttle for screening on a DM6 cryogenic light microscope (Leica Microsystems) to verify the integrity of the samples following vitrification.

Cryo-FIB Lamella preparation of pseudovirus-infected cells

After cryo-LM screening, autogrids were transferred to an Aquilos-2 cryogenic focused ion beam scanning electron microscope (cryo-FIB-SEM) (Thermo Fisher Scientific). Lamella sites were chosen based on the cell membrane signal obtained from the DM6 cryo-Light microscope (Leica Microsystems) correlated with the SEM images using MAPS 3.14 software, version 3.14.11.45 (Thermo Fisher Scientific). A total of 30 cells incubated with pseudovirus were prepared using either the manual interface (XT User: v20.1.0 - 20.1.0.7012) or semi-automated

software (AutoTEM 2.2.0 core 10.0.3) (Thermo Fisher Scientific) in the Aquilos-2 cryo-FIB-SEM. Briefly, cells were coated with an organometallic platinum layer for 12 s and gradually thinned in 4 steps at a stage angle of 15–18° using a Ga^+ beam to yield lamellae with 200-300 nm thickness after the final milling step. Micro-expansion joints were used to improve lamella stability. Progress was monitored by SEM imaging at 2–10 kV with an Everhart-Thornley Detector (ETD) detector. The final polishing step was performed manually.

Cryo-ET data collection of pseudovirus-infected cells

For pseudovirus-infected cells and lamellae, cryo-ET data were collected either using SerialEM on a Titan Krios G3i (Thermo Fisher Scientific) operated at 300kV, equipped with a K3 direct electron detector with a BioQuantum energy filter (Gatan Inc.) with energy slit set to 20 eV or a Glacios microscope (Thermo Fisher Scientific) operated at 200kV, equipped with a Falcon 3EC direct electron detector (Thermo Fisher Scientific). The autogrids were rotated 90° between Aquilos-2 and the respective electron microscope to optimize the relationship between the tilt-axis and the lamella orientation. Both instruments were operated in parallel beam condition. For each grid, an overview image (atlas) of the entire grid was acquired to locate lamellae or pre-screened cells for direct imaging. Markings on the Finder grids, which are visible in light microscopy and cryo-ET imaging modalities were used for guidance. Low-resolution images of the grid squares (pixel size 14-28 nm) containing the identified cells or lamellae enabled alignment of light microscopy and cryo-tomography images of the same cell[12]. Following correlative identification of regions of interest, dose-symmetric tilt series (± 60°, every 3°) were collected in batch mode under minimal dose conditions of about 90-120 $e^-/Å^2$ with defocus between 8 and 14 µm and a magnification resulting in a calibrated pixel size of 0.48 nm.

Cryo-ET data processing

Automated real-time reconstruction protocols as implemented in the pyCoAn package, version 0.3 (github.com/pyCoAn/distro), an extended python version of the CoAn package[13] were employed for all reconstructions. Briefly, immediately after acquisition, tilt series were automatically aligned[14] and then reconstructed using the Simultaneous Iterative Reconstruction technique[15]. Alignment and reconstruction statistics were used to determine quality scores that are provided in real time during data collection. Some of the lamellae tilt series were also reconstructed using EMAN2[16], version 2.9. A total of 387 cellular tomograms were acquired and analysed. Pseudovirus was detectable by their distinct structural signature in 181 tomograms. For the analysis of MLV-based particles, 35 tomograms with pseudovirus only, 83 tomograms with hACE2 nanoparticles only and 71 tomograms with a mixture of both were acquired and analysed. Interactions between hACE2 nanoparticles and pseudoviruses were analysed from unfixed samples only. Segmentation of features of interest was achieved using manual tracing with Amira[17], version 2019.4. The reconstructions were denoised either with Topaz[18], version 0.2.5-2, or non-local means[19] followed by a Wiener-like filter accounting for the contrast transfer function at the respective defocus and an estimate of the spectral signal-to-noise ratio[20] as implemented in pyCoAn. Tomogram slices were visualized with IMOD[21], version 4.11.1, and segmentation results with Amira.

Sub-tomogram averaging of hACE2 nanoparticles

Sub-tomogram averaging of hACE2 particles on hACE2 nanoparticles was performed following the EMAN2 sub-tomogram averaging pipeline[22]. Briefly, tilt series from hACE2 nanoparticle

samples with high quality alignment scores and good visibility of protruding particles were binned by two, imported into EMAN2, reconstructed, and the contrast transfer function parameters were estimated for each reconstruction. 311 particles protruding from the membrane and showing good separation from their neighbours were manually selected. After initial alignment and sub-tomogram averaging, the particles were manually curated according to the quality of their fit, leaving 207 particles for the subsequent analysis. These particles were subjected to the sub-tomogram refinement routines in EMAN2, resulting in a final sub-tomogram average of 2.7-nm resolution. The density showed clear evidence for a two-fold symmetry and was symmetrized accordingly for comparison with the hACE2 dimer structure. The hACE2 dimer structure was extracted from the open conformation of the hACE2-B0AT1 complex[23] (PDB: 6MD1) and fitted and compared to the density using Chimera[24], version 1.15, which was also used to render the images of the density and the atomic model.

Data availability

The datasets generated during and/or analysed during the current study are available from the corresponding author on reasonable request.

METHODS REFERENCES:

1. Shang, J. et al. Structural basis of receptor recognition by SARS-CoV-2. *Nature* **581**, 221-224 (2020).
2. Millet, J. K. & Whittaker, G. R. Murine Leukemia Virus (MLV)-based Coronavirus Spike-pseudotyped Particle Production and Infection. *Bio Protoc* **6**, (2016).
3. Matsuyama, S. et al. Enhanced isolation of SARS-CoV-2 by TMPRSS2-expressing cells. *Proc Natl Acad Sci U S A* **117**, 7001-7003 (2020).
4. Hui, K. P. Y. et al. Tropism, replication competence, and innate immune responses of the coronavirus SARS-CoV-2 in human respiratory tract and conjunctiva: an analysis in ex-vivo and in-vitro cultures. *Lancet Respir Med* **8**, 687-695 (2020).
5. Chan, M. C. et al. Tropism and innate host responses of a novel avian influenza A H7N9 virus: an analysis of ex-vivo and in-vitro cultures of the human respiratory tract. *Lancet Respir Med* **1**, 534-542 (2013).
6. Hui, K. P. et al. Tropism and innate host responses of influenza A/H5N6 virus: an analysis of ex vivo and in vitro cultures of the human respiratory tract. *Eur Respir J* **49**, (2017).
7. Kärber, G. Beitrag zur kollektiven Behandlung pharmakologischer Reihenversuche. *Naunyn-Schmiedebergs Archiv für experimentelle pathologie und pharmakologie* **162**, 480-483 (1931).
8. Schindelin, J. et al. Fiji: an open-source platform for biological-image analysis. *Nat Methods* **9**, 676-682 (2012).
9. Mastronarde, D. N. Automated electron microscope tomography using robust prediction of specimen movements. *J Struct Biol* **152**, 36-51 (2005).
10. Hagen, W. J. H., Wan, W. & Briggs, J. A. G. Implementation of a cryo-electron tomography tilt-scheme optimized for high resolution subtomogram averaging. *J Struct Biol* (2016).
11. Gaietta, G., Swift, M. F., Volkmann, N. & Hanein, D. Rapid tool for cell nanoarchitecture integrity assessment. *J Struct Biol* **213**, 107801 (2021).

12. Anderson, K. L., Page, C., Swift, M. F., Hanein, D. & Volkmann, N. Marker-free method for accurate alignment between correlated light, cryo-light, and electron cryo-microscopy data using sample support features. *J Struct Biol* **201**, 46-51 (2018).
13. Volkmann, N. & Hanein, D. Quantitative fitting of atomic models into observed densities derived by electron microscopy. *J Struct Biol* **125**, 176-184 (1999).
14. Mastronarde, D. N. & Held, S. R. Automated Tilt Series Alignment and Tomographic Reconstruction in IMOD. *J Struct Biol* **197**, 102-113 (2016).
15. Agulleiro, J. I. & Fernandez, J. J. Fast tomographic reconstruction on multicore computers. *Bioinformatics* **27**, 582-583 (2011).
16. Tang, G. et al. EMAN2: An extensible image processing suite for electron microscopy. *J Struct Biol* **157**, 38-46 (2006).
17. Stalling, D., Hege, H. C. & Westerhoff, M. in *Visualization Handbook* (eds Johnson, C. R. & Hansen, C. D.) (Academic Press, 2004).
18. Bepler, T., Kelley, K., Noble, A. J. & Berger, B. Topaz-Denoise: general deep denoising models for cryoEM and cryoET. *Nat Commun* **11**, 5208 (2020).
19. Buades, A., Coll, B. & Morel, J.-M. A non-local algorithm for image denoising. *Proc IEEE Comput Soc Conf Comput Vis Pattern Recognit* **2**, 60-65 (2005).
20. Tegunov, D. & Cramer, P. Real-time cryo-electron microscopy data preprocessing with Warp. *Nat Methods* **16**, 1146-1152 (2019).
21. Kremer, J. R., Mastronarde, D. N. & McIntosh, J. R. Computer visualization of three-dimensional image data using IMOD. *J Struct Biol* **116**, 71-76 (1996).
22. Chen, M. et al. A complete data processing workflow for cryo-ET and subtomogram averaging. *Nat Methods* **16**, 1161-1168 (2019).
23. Yan, R. et al. Structural basis for the recognition of SARS-CoV-2 by full-length human ACE2. *Science* **367**, 1444-1448 (2020).
24. Goddard, T. D., Huang, C. C. & Ferrin, T. E. Visualizing density maps with UCSF Chimera. *J Struct Biol* **157**, 281-287 (2007).

ACKNOWLEDGEMENTS

We are grateful to Jean Dubuisson and Muriel Lavie (Institut Pasteur de Lille) for sharing pCMV-MLV-gag-pol and pTG-Luc plasmids for the MLV pseudotyping system and for their continued support and advice, to Ignacio Fernández and Félix Rey (Institut Pasteur) for providing soluble, cytoplasmic hACE2 protein samples, to Nicolas Escriou (Institut Pasteur) for providing pCI-SARS2-Spike plasmid, and to Pedro Alzari and the Structural Microbiology Unit (Institut Pasteur) for providing access to rotors and chemicals. We are grateful to Ko-Yung Sit (University of Hong Kong), Michael KY Hsin, and Timmy WK Au (Department of Surgery, Queen Mary Hospital) for their assistance with the *ex-vivo* assays. We acknowledge access to the Leica plunge freezer at the Ultrastructural Bioimaging facility of Institut Pasteur and the Titan Krios, Glacios, Vitrobot, and Aquilos-2 instruments at the NanoImaging Core of the Institut Pasteur. The NanoImaging Core at Institut Pasteur was created with the help of a grant from the French Government's Investissements d'Avenir program (EQUIPEX CACSICE - Centre d'analyse de systèmes complexes dans les environnements complexes, ANR-11-EQPX-0008). We are in debt to Olivier Le Bihan, Maria Girleanu, and Anne Laure Favier (Département des Plateformes et Recherche Technologique, Unité Imagerie at Institut de Recherche Biomédicale des Armées; IRBA) for support and assistance during the sample preparation and data collection

at IRBA. The research work in Hong Kong was funded by the National Institute of Allergy and Infectious Diseases, National Institutes of Health, Department of Health and Human Services (Contract No. 75N93021C00016) and the Theme-Based Research Scheme (Ref: T11-705/21N and T11-712/19-N) under University Grants Committee of Hong Kong Special Administrative Region. The initial phase of setting up the cell and pseudovirus systems was supported by the "URGENCE COVID-19" fundraising campaign of Institut Pasteur (DH, NV).

AUTHOR CONTRIBUTIONS

DH and NV conceived, directed, and supervised this project. CS, ML, AB, BRdF set up, applied, and refined the methodology, visualization, and analysis. MC, KH, KN and JN performed the *ex-vivo* assays. All authors reviewed and provided input to the manuscript.

DECLARATION OF INTERESTS

The authors declare no competing interest

CORRESPONDING AUTHOR

Correspondence and requests for materials should be addressed to Niels Volkmann (niels.volkmann@pasteur.fr).

EXTENDED DATA

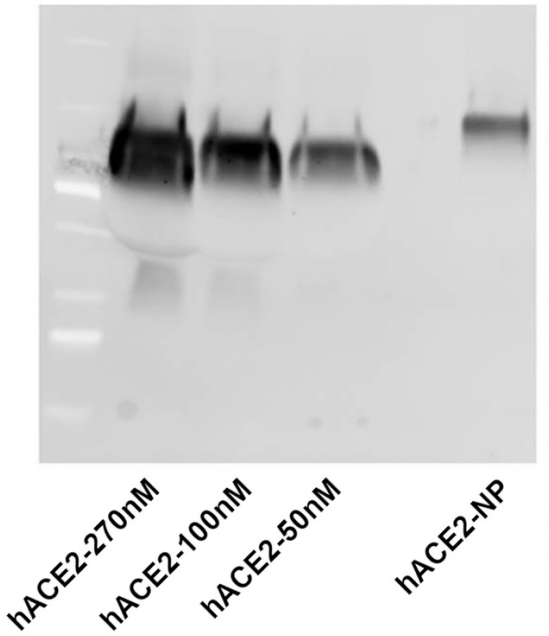

Extended Data Figure 1: Quantification of hACE2 in nanoparticles. Representative western blot used for quantification of hACE2 levels in hACE2 nanoparticles (hACE2-NP) using soluble hACE2 at different concentrations (hACE2-…nM).

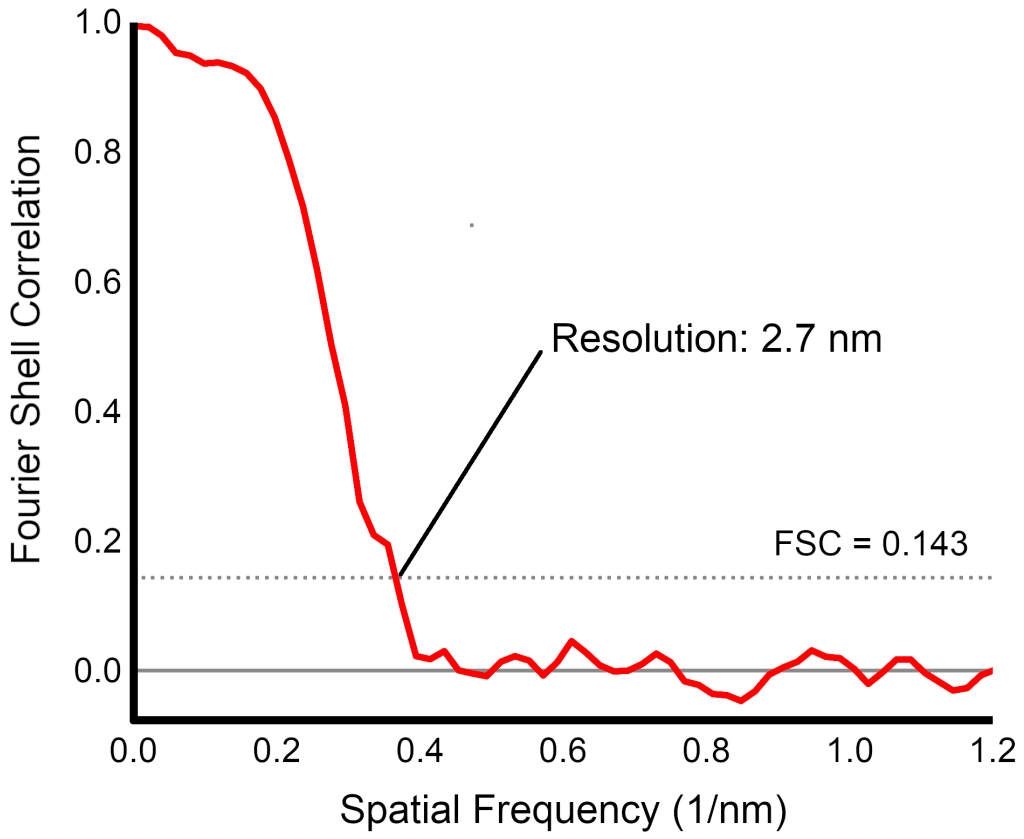

Extended Data Figure 2: Resolution assessment of nanoparticle-bound hACE2 sub-tomogram average. The data was split in half and refined independently as part of the EMAN2 pipeline. The resolution estimate is then given as the value were the Fourier Shell Correlation (FSC) between the two halves falls below 0.143.